Zhao Zhu[1], Maximiliano J. Bezada[1], Joseph S. Byrnes[1*], Heather A. Ford[2]

[1]Department of Earth & Environmental Sciences, University of Minnesota, Twin Cities

[2]Department of Earth and Planetary Sciences, University of California, Riverside

*Now at Northern Arizona University

Corresponding author: Zhao Zhu (zhu00064@umn.edu)

Key Points:

- Deformation in the Rocky Mountain Front is highly correlated with high Δt^*.
- Laramide-Style deformation may be caused by variations in lithospheric strength and thickness.
- Stress may be localized in weaker lithosphere to form Laramide-style ranges.

Abstract

The Wyoming Craton underwent tectonic modifications during the Laramide Orogeny, which resulted in a series of basement-cored uplifts that built the modern-day Rockies. The easternmost surface expression of this orogeny - the Black Hills in South Dakota - is separated from the main trend of the Rocky Mountains by the southern half of the Powder River Basin, which we refer to as the Thunder Basin. Seismic tomography studies reveal a high-velocity anomaly which extends to a depth of ~300 km below the basin and may represent a lithospheric keel. We constrain seismic attenuation to investigate the hypothesis that the variations in lithospheric thickness resulted in the localization of stress and therefore deformation. We utilize data from the CIELO seismic array, a linear array that extends from east of the Black Hills across the Thunder Basin and westward into the Owl Creek Mountains, the BASE FlexArray deployment centered on the Bighorn Mountains, and the EarthScope Transportable Array. We analyze seismograms from deep teleseismic events and compare waveforms in the time-domain to characterize lateral varations in attenuation. Bayesian inversion results reveal high attenuation in the Black Hills and Bighorn Mountains and low attenuation in the Thunder and Bighorn basins. Scattering is rejected as an confounding factor because of a strong anticorrelation between attenuation and the amplitude of P wave codas. The results support the hypothesis that lateral variations in lithospheric strength, as evidenced by our seismic attenuation measurements, played an important role in the localization of deformation and orogenesis during the Laramide Orogeny.

1 Introduction

Cratons, the cores of continents, typically resist tectonic deformation and are devoid of contemporary seismic and magmatic activity (e.g. Lee et al., 2011).

Nevertheless, geophysical and geological observations indicate that cratons can be subject to the destructive effects of tectonic and mantle dynamics. Examples of this include the North China Craton (e.g. Gao et al. 2004; Kusky & Li 2003; Zhu et al. 2012), the Dharwar Craton (Griffin et al., 2009), and the Brazilian Shield (Beck & Zandt, 2002; Kusky et al., 2014; Ramos et al., 1986). The circumstances that enable intracratonic deformation are debated, including the loss of their lithospheric keel caused by gravitional instabilities or convection (e.g. Conrad & Molnar, 1997; Huang et al., 2003), the rheological weakening of cratonic mantle due to rehydration (e.g. Humphreys et al., 2003), and other scenarios where the lithospheric mantle is modified.

The Wyoming Craton remained relatively immune to modification until its recent reactivation, which refers to the lithospheric thinning associated with the change of tectonic environment (Wang et al., 2013). After formation by the cratonization of Neoarchean volcanic arcs (Mueller & Frost, 2006) and accretion to the core of the North American Shield at ~1.8 Ga (Whitmeyer & Karlstrom, 2007), the craton experienced a long period of quiescence which ended with the onset of the Laramide Orogeny at 80 Ma. At that time, the shallow subduction of the Farallon Plate resulted in strong horizontal stress on the Wyoming Craton, causing the contraction of the crust by 50-60km through a series of deep-seated, basement involved thrust faults (Bird, 1998; Coney & Reynolds, 1977; DeCelles et al., 1991; Dickinson & Snyder, 1978; Fan & Carrapa, 2014; Humphreys et al., 2015; Saleeby, 2003). The orogeny uplifted widespread foreland arch systems, including the Bighorn Mountains and the Black Hills. The southern portion of the relatively flat Powder River Basin extends between these two ranges. To avoid confusion with the greater Powder River Basin, we refer to this southern extension as the Thunder Basin after the National Grassland of that name which occupies the area. Similar to the Black Hills – Thunder Basin pair, the Bighorn Mountains are flanked to the west by Bighorn Basin. This pattern of intermittent landforms composes much of the Rocky Mountains: discrete basement-cored uplifts away from the plate boundary, and has come to be known as Laramide Style deformation (Fig. 1).

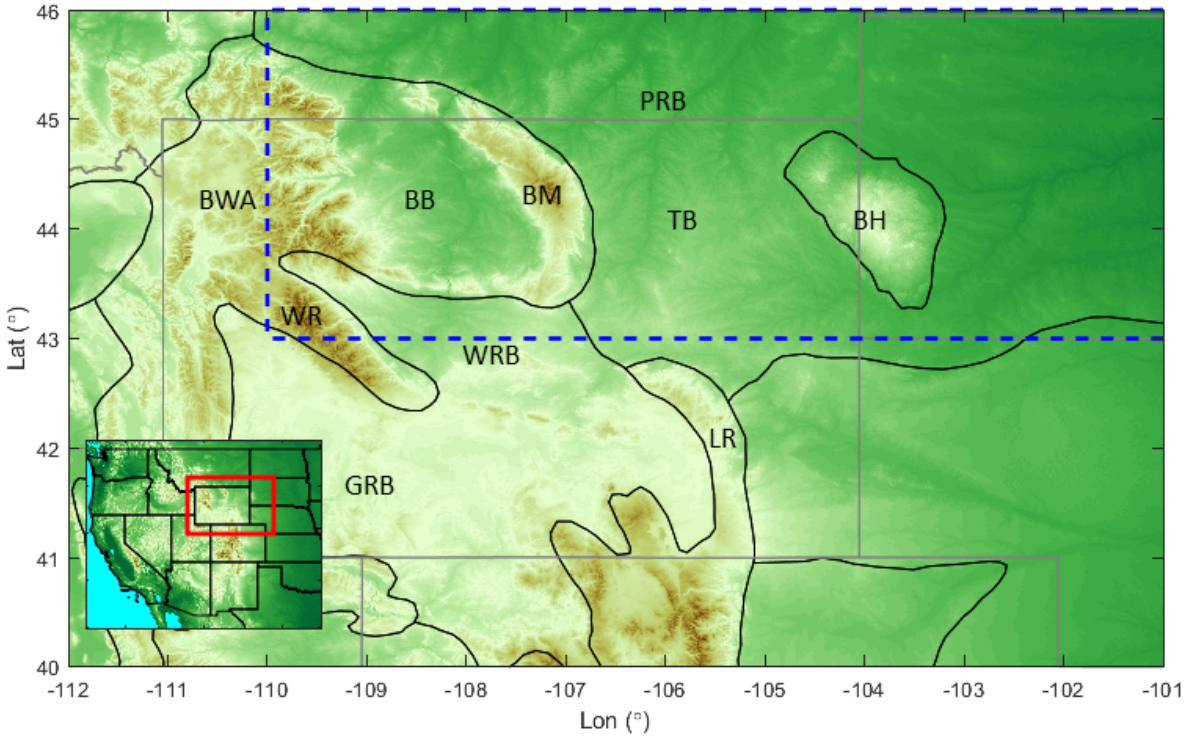

Figure 1. Physiographic provinces of the Rocky Mountains Front in the region surrounding the State of Wyoming (BB: Bighorn Basin, BH: Black Hills, BM: Bighorn Mountains, BWA: Beartooth-Washakie-Absaroka Ranges, GRB: Green River Basin, LR: Laramie Range, PRB: Powder River Basin, TB: Thunder Basin, WR: Wind River Range, WRB: Wind River Basin); Dashed blue rectangle marks the region where relatively dense seismic arrays are present.

Important questions are still debated as to how Laramide style deformation proceeds: Why do uplifts occur in regions far inside the continent rather than close to the plate boundary? How is stress transferred among blocks and localized in certain regions? Is the variation of topography related to just to the strength of the crust or to the strength of the whole lithosphere? Do pre-existing structures influence these basement-cored uplifts?

Since the Wyoming Craton is large compared to the size of the mountain ranges contained within it, these problems have been approached from a variety of perspectives and scales. Receiver function (Yeck et al., 2014) and active source seismology studies (Worthington et al., 2016) suggest that pre-existing crustal heterogeneities or Moho topography resulted in the nucleation of foreland arches. Passive-source seismic imaging reveals a NE-trending high-velocity anomaly extending from the Moho to ~300km depth directly below the Thunder Basin

(Dave & Li, 2016; Schmandt & Humphreys, 2010; Schmandt & Lin, 2014; Shen & Ritzwoller, 2016; Wang et al., 2016). We refer to this high-velocity anomaly as the Thunder Basin Block (TBB). The TBB's anomalous velocity structure has been interpreted in several ways: Dave & Li (2016) suggested that the high-velocity anomaly may be a delaminating lithospheric keel, resulting from small scale convection originated from shallow angle subduction of the Farallon plate and the nearby Yellowstone Hotspot. In contrast, Humphreys et al. (2015) argue that the anomaly is evidence of onging recratonization by underplating the thinned lithosphere of the Wyoming Craton with the lithospheric mantle of a subducted oceanic plateau. Each of these scenarios imply different rheological conditions for this lithospheric block.

In this study, we characterize seismic attenuation in the eastern half of the Wyoming Craton and use our observations to better understand the relationship between lithosphere strength and Laramide style deformation. Observations of seismic attenuation may help to differentiate between the different hypotheses due to an integrated sensitivity to the lithosphere-asthenosphere system above a depth a of ~220 km (Castaneda et al., 2021). We would expect an intact cratonic lithosphere to demonstrate universally low attenuation, while other cases may lead to either large or small variations in attenuation depending on the thickness of the a strong lithosphere block. We show results that suggest the uplifted ranges of the Wyoming Craton are causally related to variations in lithospheric strength and thickness: regions with mountain ranges are characterized by high attenuation while nearby basins are characterized by low attenuation. From this perspective, Laramide style deformation may be a result of lateral stress transfer among pre-existing lithospheric blocks with distinct thickness and strength.

2 Data and Methods

2.1 Why Attenuation?

Although the processes that control seismic attenuation are debated, seismic attenuation can provide a constraint on lithospheric strength independent from constraints on seismic velocity (Jackson & Faul, 2010; Karato, 2008). The attenuation of a seismic wave is the loss of energy during propagation. A perfectly elastic medium does not attenuate seismic waves, but real "anelastic" materials contain imperfections that result in attenuation. As the wave propagates through regions with greater anelasticity, high-frequency energy is preferentially removed, resulting in a broadening of the waveforms. This effect is quantified by the parameter t*, which represents the integrated effect of attenuation over the entire raypath:

$$t^* = \int \frac{\mathrm{dt}}{Q} = \int \frac{\mathrm{dx}}{c(x)Q(x)}$$

where Q is the quality factor, and c is the seismic wave velocity. A perfectly elastic material has infinite quality factor. While measuring t* directly requires

detailed knowledge of the source, the difference in t* for phases from the same source along different raypaths (Δt*) can be readily estimated. Since we measure the path-integrated attenuation, we have no direct constraint on where along the ray attenuation occurred, and the relative scarcity of data in the teleseismic case typically precludes a tomographic approach. However, given the very large difference in Q between the lithosphere and the low-viscosity asthenosphere (e.g. Dziewonski & Anderson 1981; Montagner & Kennett 1996) we assume the variations in t* stem from the differences in lithospheric thickness among regions: Higher t* values (positive Δt*) suggest thicker and stronger lithosphere blocks compared to regions with lower t* (negative Δt*). This assumption is in line with recent results from Alaska (Castaneda et al., 2021) and northern China (Liu et al., 2021) which show that attenuation measurements are most sensitive to structure below the crust and above ~220 km depth.

2.2 Data

To gain a better understanding of the lithospheric strength variations between the Black Hills, the Thunder Basin, and surrounding areas, we deployed a line of 24 broadband seismic stations spanning the region, that we refer to as the CIELO (Crust-Lithosphere Investigation of the Easternmost Expression of the Laramide Orogeny) array (Fig. 2). Along with existing data from the EarthScope Transportable Array (TA) and the Bighorn Arch Seismic Experiment (BASE, Sheehan, 2009) which covers the NW of our study area, we are able to collect ~2000 P wave arrivals from 48 deep events (hypocenter deeper than 250km and magnitude greater than Mb5.5, Fig. 3). Seismic rays from deep events have the advantage that they only travel through the low-Q asthenosphere on the receiver side. The majority of our events come from the subduction zones located in Northeast Asia and South America, with a small number from Tonga and Western Europe (Fig. 3), providing good backazimuthal coverage when compared to similar studies (Bezada, 2017; Byrnes et al., 2019).

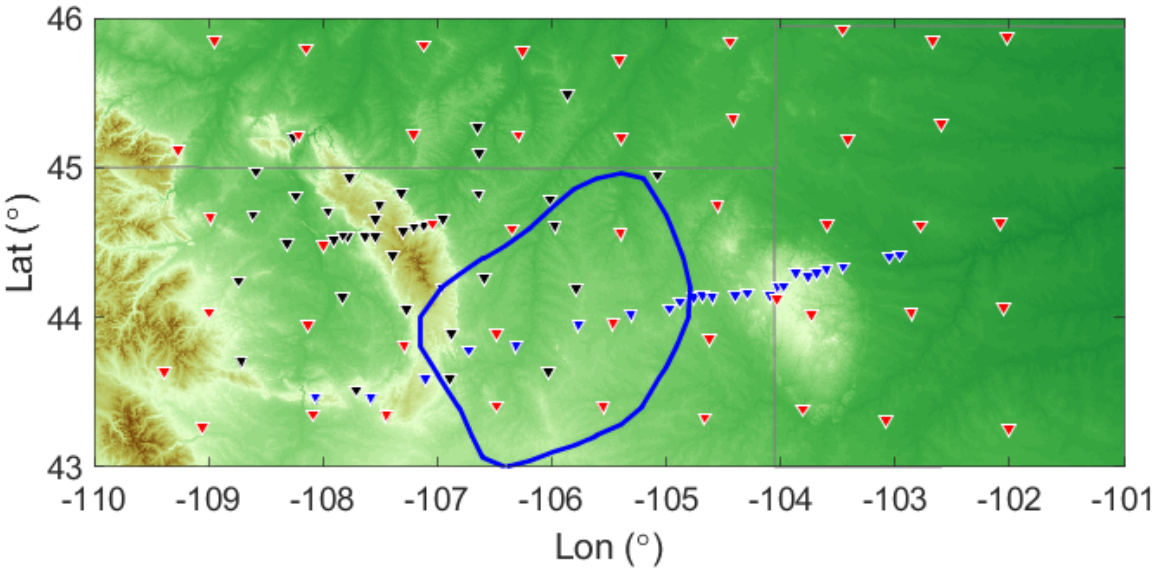

Figure 2. The location of seismic arrays in the region marked by blue dashed rectangles in figure 1. Blue contour marks the boundary of a 2% high dVp anomaly in the velocity model of Schmandt and Lin (2014) at the depth of 200km

2.3 Time Domain Measurement of Δt*:

We adopt the time domain Δt* measurement method introduced in Bezada (2017) as it appears to be more robust with respect to confounding factors such as the scattering of seismic energy compared to the traditional spectral ratio method of Teng (1968) (Bezada et al., 2019; Byrnes et al., 2019). First, we produce an estimate of the unattenuated source seismic waveform for each event. We do this by selecting and stacking the seismic traces with the most impulsive first arrivals and the most high-frequency energy. We find Δt* for each recorded trace by comparing it with a numerically attenuated version of the source waveform estimate produced with the attenuation operator of Azimi (1968) in the frequency domain:

$$A = exp\{-\omega\, t^* \bullet [\frac{1}{2} + \frac{i}{\pi} \ln\left(\frac{\omega}{\omega_0}\right)]\}$$

where only the the factor t^* has an impact on relative observations. We grid-search over Δt* values and choose the value that minimizes the L_2 norm of the misfit between the numerically attenuated source trace and the observed waveform in a selected window in the time domain. Results are culled by visually inspecting each best-fit attenuated waveform. A demonstration of acceptance

and rejection criteria can be found in Fig 4. In this way, we obtained 1489 Δt^* measurements from 137 stations after quality control.

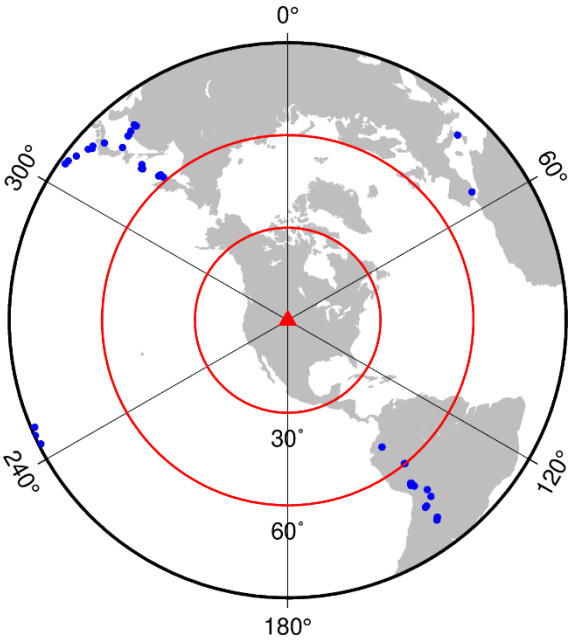

Figure 3. The deep events (depth>=200km, Mw>=5.5) that are picked up by the seismic networks in our study

2.4 Inversion Approach

Due to the limited number of available events and seismic waveforms, it is not feasible to constrain a 3D model for the entire region. Instead, we invert for a 2D (map-view) model of lateral variations in attenuation.

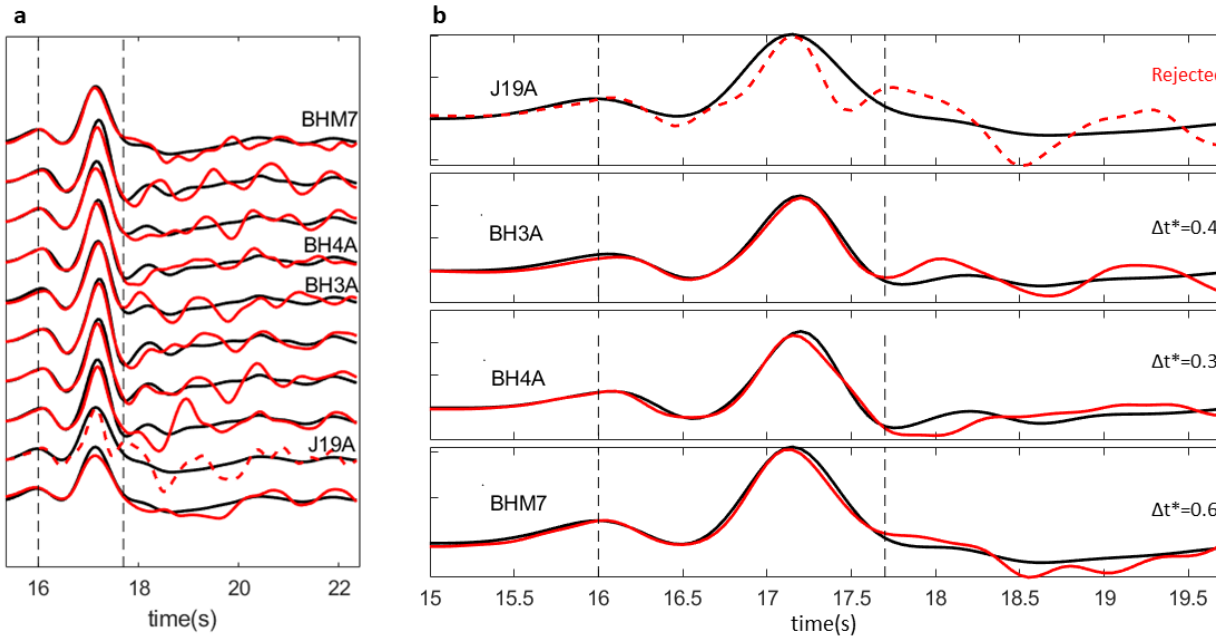

Figure 4. (a)Delta t* measurement results for one of the events picked up by TA and BASE array(b) the waveform matching results for the stations marked in (a), where the traces plotted in red represent the synthetic data attenuated from the prototype source trace, and the black traces are the waveform from the stations. The delta t* measurement on station TA.J19A is rejected due to the low correlation between synthetic data and observed data.

We use the Markov Chain Monte-Carlo (MCMC) approach described in Byrnes et al. (2019) to invert for a map of lateral variations in attenuation. A linear inversion for this type of dataset (Bezada, 2017) requires subjective hyperparameters such as damping and smoothing factors which have non-negligible impacts on the inverted model (Fig. S1). Bayesian approaches based on MCMC offer a useful alternative that introduce minimal external constraints (e.g. Bodin et al. 2012; Malinverno & Briggs 2004; Ravenzwaaij et al. 2014). At the beginning of the inversion, several independent chains are initialized with models described by a random number of nodes with stochastically generated Δt^* values. Five possible manipulations to each model can occur, including 1) generating a new node; 2) removing an existing node; 3) changing the value of Δt^* of a node; 4) moving an existing node to a different location; 5) perturbing the uncertainty of the data. New models are always accepted if they have an equal or lower misfit than the previous model, or have a non-zero probability of being accepted even if their misfit is higher (Byrnes & Bezada 2020). Since the starting model is randomly generated, we set an empirical "burn-in" stage during which we do not keep the generated models. After the overall misfit of the model decreases

sufficiently during the burn-in period (Fig. S2), we keep one out of every 100 models to reduce the redundancy of the model set. The number of chains and iterations have an impact on the overall results, but models generally agree with each other on the location and magnitude of anomalies (Fig. S3). Based on several trial inversions (Fig. S4), we chose to perform 10^6 iterations over 30 chains.

2.5 Scattering Observations

As discussed above, more attenuated seismic waveforms appear broader since high-frequency energy has been absorbed by the propagation medium. Unfortunately, other wave propagation phenomena can mimic this effect on the waveform. In particular, the scattering of seismic energy off small-scale heterogeneities may alter the seismic wavefield by delaying the arrival of high frequency seismic energy. Possibily, then, the apparent attenuation of the waveforms in our study could be an artefact caused by scattering. For example, Cafferky & Schmandt (2015) pointed out that the scattering of energy from dipping interfaces may exaggerate the Δt^* variations measured by the frequency-domain method, as indicated by the presence of a significant amount of high-frequency energy on the transverse component.

Given these considerations, we make an additional measurement described in Bezada (2017) to quantify the scattering of seismic energy at each station. The strength of the high-frequency coda in the waveforms is measured by what we refer to as the scattering index, which quantifies the amount of energy preserved after a high-pass filter is applied to the time window containing the coda. The seismic coda that lies in the 10-s window after the P arrival is high-pass filtered with a corner frequency of 4 Hz. To reduce the influence of noise, we subtract the envelope of data in a 10 s window 5 s before the P arrival. The index is then the ratio between the envelopes of filtered and unfiltered traces. Larger index values reflect more high-frequency energy transferred to the P wave coda. To demonstrate the distribution of scattering magnitude, we invert the measurements with the same MCMC approach as used for the attenuation observations.

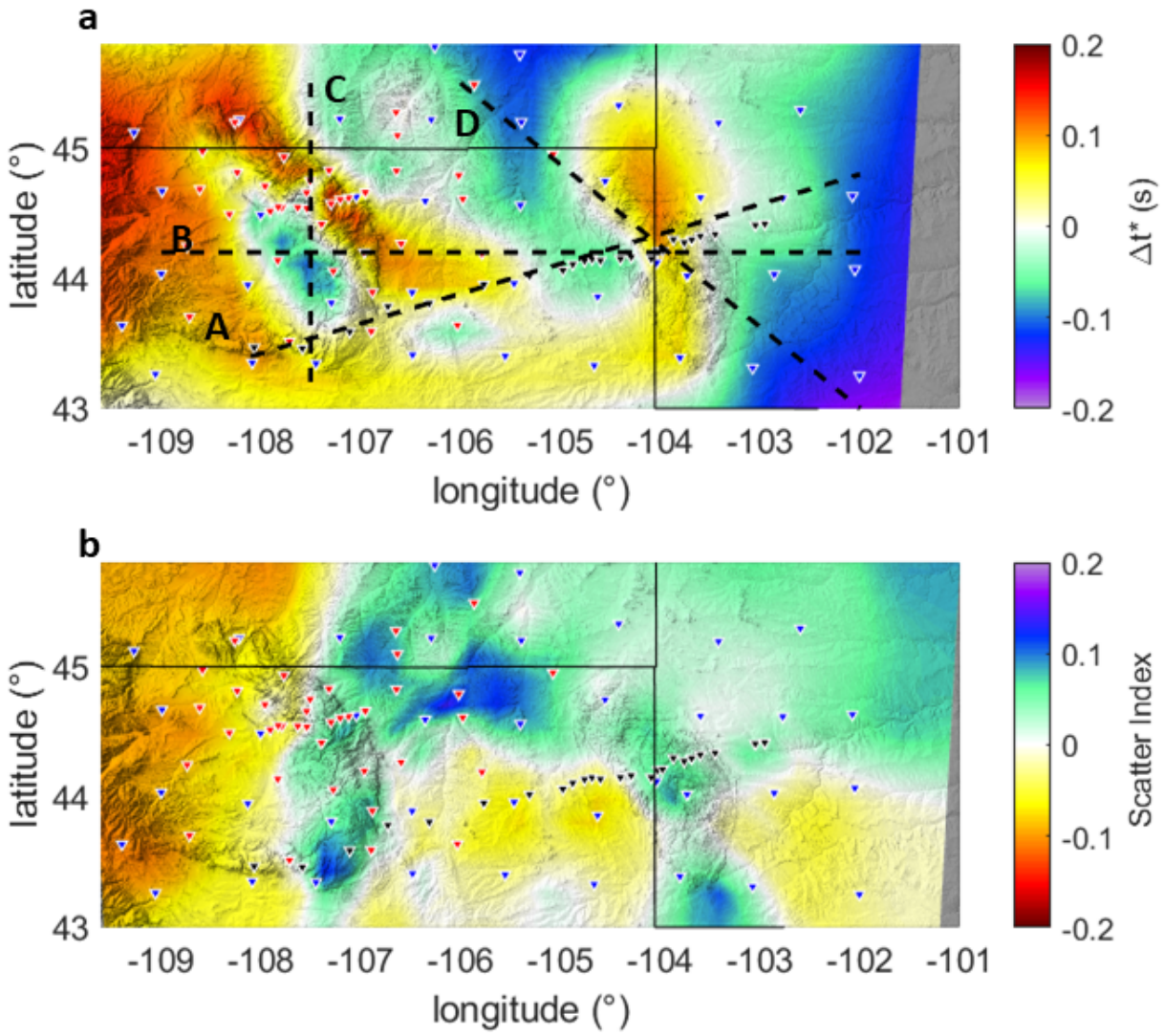

Figure 5. (a) Preferred MCMC inversion result with 30 chains and 1e6 iterations on each chain. The Δt^* is shown in color overlaid on the shaded relief topography (Etopo1). Triangles mark the locations of seismic stations: blue: TA stations; red: BASE stations; black: CIELO stations. Dashed lines indicate the locations of cross-sectional plots shown in Figure 7; (b) Preferred MCMC inversion result (30 chains, 1e6 iterations) of the scattering index. Magnitude of the scattering index is colorcoded with the corresponding colors in colorbar

3 Results

Fig 5a shows the mean of the ensemble models for Δt^*. To first order, regions

that are considered to be part of the interior of Laurentia (the northern and eastern parts of the study area) show overall low Δt^*, as much as -0.15s, indicating weak attenuation. In contrast, the main trend of the Rocky Mountains lying in the west end of the study area shows high Δt^* (~0.2s) values, indicating strong attenuation. The Wyoming Craton does not demonstrate universally high or low Δt^* values: basins (such as the Thunder Basin (TB) and Bighorn Basin (BB)) display low Δt^* (approximately -0.1s) and the highest Δt^* (0.1s – 0.2s) are clustered around the mountain ranges (Bighorn Mountains (BM), Windriver Ranges (WR), and the Black Hills (BH)).

Our analysis of potential confounding factors leads us to conclude that the Δt^* model primarily reflects intrinsic attenuation. The Δt^* variation positively correlates with topography in the region (correlation coefficient of 0.61, Fig. S5). On the other hand, our map of scattering intensity (Fig 5b) anti-correlates (-0.51) with the Δt^* model. This pattern precludes extrinsic attenuation due to scattering as a first order contribution to variations in Δt^*. For instance, regions with higher Δt^* values coincide with low scattering index (e.g. the Bighorn Mountains, the Beartooth-Washakie-Absaroka Ranges, Fig. 5), indicating the high frequency energy was absorbed rather than scattered. Although it has been suggested that mountain ranges may lead to stronger scattering effects due to the prevalence of dipping surfaces (Cafferky & Schmandt, 2015), we do not observe this. The gradient of the topography and surface roughness (Fig. S5) both showed little correlation with the scattering index, implying the topography is not a major driver of scattering in this region. It has also been suggested that an as-yet unidentified wave propagation phenomenon may lead to artificially low Δt^* within basins (Castaneda et al., 2021), and we do indeed observe low Δt^* in basins in this study. We note, however, that previous results show that our methodology for measuring Δt^* does not universally assign high values to mountainous regions and low values to basins. Byrnes & Bezada (2020) observed a high Δt^* anomaly in the Salton Trough, a low-lying and flat basin, while Deng et al. (2021) observed a local minimum in Δt^* in the rugged mountainous ranges of the Chuan-Dian Block in southwestern China.

In addition, the ensemble model has an overall low uncertainty (~0.06s) relative to the magnitude of the anomalies (Fig. 6a). Where stations are more densly distributed, the standard deviations typically fall to approximately 0.04s, while uncertainties tend to be higher near the boundary of distinct Δt^* anomalies (~0.08s). A detailed look at the Δt^* distribution among different models can be found in Fig. 6b, where the mean of the ensemble models fits well with the estimates with highest probability, consistent with the absence of significant skew in the distributions.

As a check on the Bayesian model, we also inverted the quality-controlled data with the linear inversion approach (Text S1, Fig. S6). We chose the hyper-parameters based on the tradeoff between model norm and misfit to the data. The outline and magnitude of Δt^* anomalies in the Bayesian model and our preferred linear inversion are highly similar (Fig. S6 and Fig. S3) and would

lead to the same general conclusions. We choose the Bayesian model as our preferred model because it more adequately handles observation uncertainty, which it determines to be ~0.15 s.

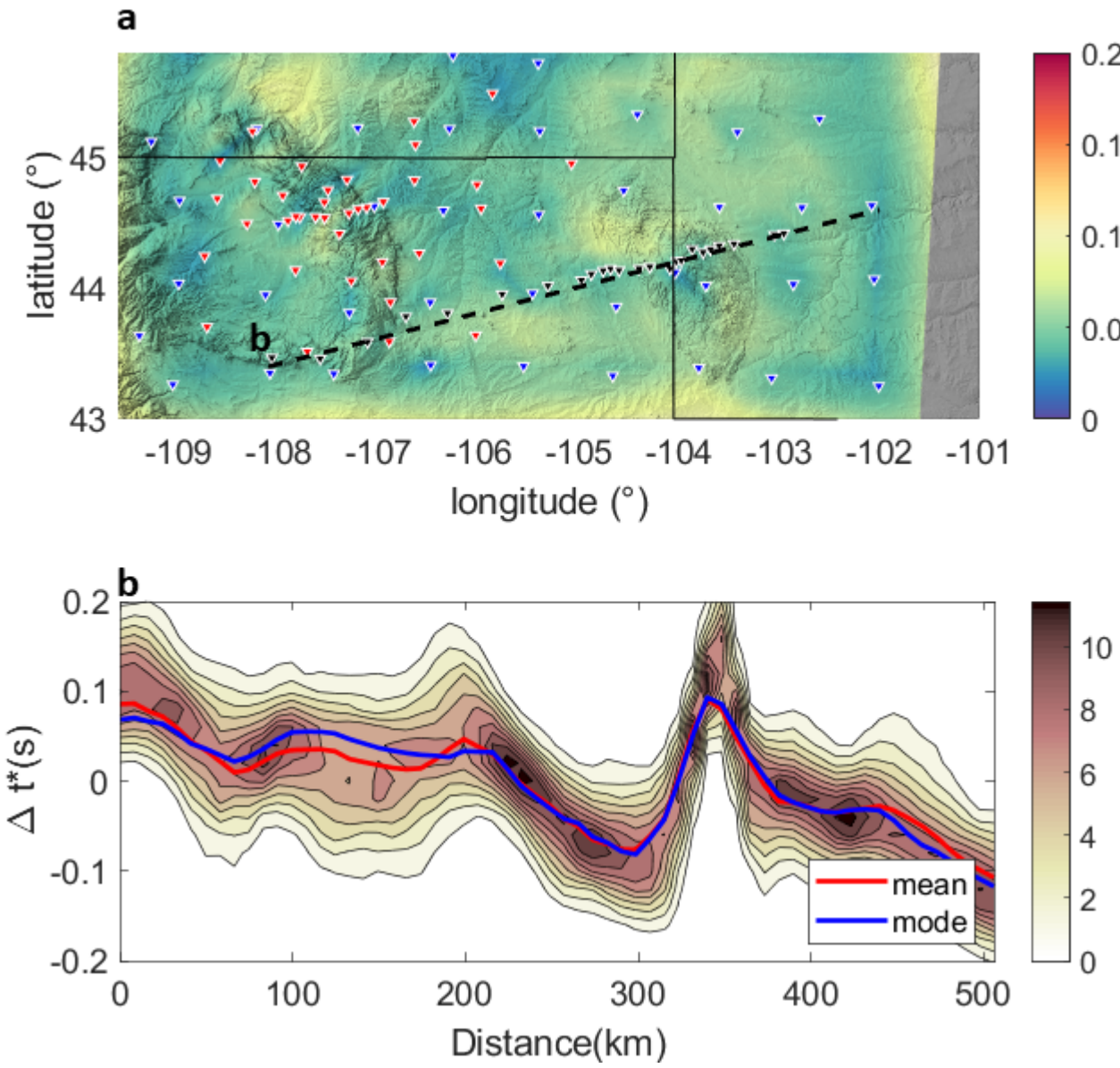

Figure 6. (a) Standard deviation of Δt* among the preferred ensemble of models (b) probability density distribution of Δt* among the ensemble of models along the dashed line in (a); the red and blueline show the average and most frequent Δt* value of the ensemble of models, respectively

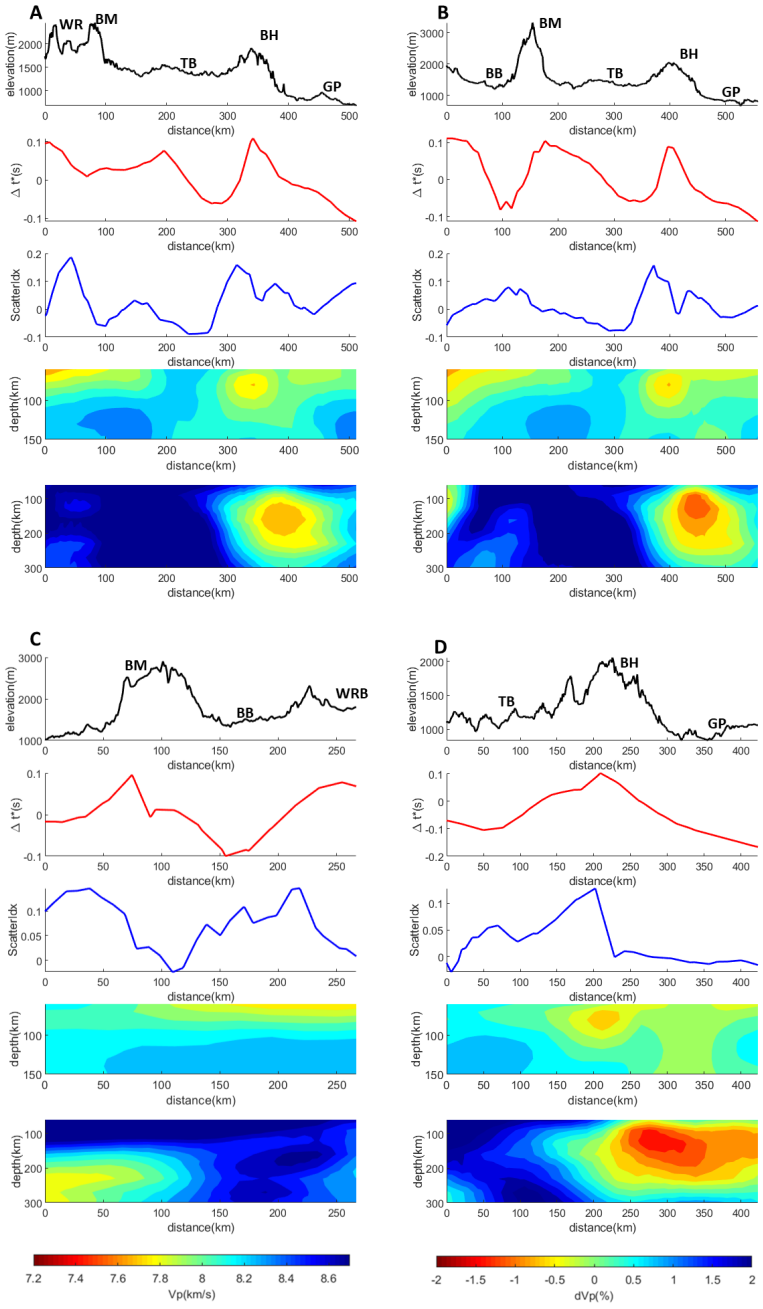

Figure 7. Elevation, Δt* values, Scattering Index, vp model (SL14), dvp model

(SR16) along the lines shown in Figure 5

The uncertainty in the data may reflect a random component in the measurement, or be related to systematic differences between different subsets of events. We explore subsets of events in Fig. S7. We produced two models, KM and SAM, by inverting data from the Kurils and South America, respectively. While KM and SAM show a similar trend of Δt^* (high to low from west to east), the magnitude of Δt^* at the TBB in the KM (~0s) is much smaller than that of SAM (~-0.1s). The reason behind this difference may be the attenuation in the deeper Earth sampled differently by the raypaths, since the backazimuth of the event sets vary drastically. Nevertheless, the overall pattern of Δt^* is consistent with our preferred model and neither subset would lead to different general interpretations.

4 Discussion

4.1. Overall Variation of Δt^*

Lateral variations in attenuation likely reflect variations in the thickness of the lithosphere or the quality factor of the asthenosphere beause of the drastic contrast in Q of the lithosphere and asthenosphere in 1D Earth models (Dziewonski & Anderson, 1981; Montagner & Kennett, 1996; Romanowicz & Dziewonski, 2010). Our observation of the transition of Δt^* from west to east agrees well with existing Δt^* models (Cafferky & Schmandt, 2015), LAB depth transition implied by observations of heat flow (Blackwell et al., 2011) and seismic velocity models (e.g. Porter et al., 2016; Schmandt & Lin, 2014; Shen & Ritzwoller, 2016; Xie et al., 2018). The most tectonically active regions of the study area, primarily in the Rocky Mountains, feature higher Δt^* values, which agrees with the expectation of thinned lithosphere in these areas following the flat subduction of Farallon Slab (e.g. DeCelles 2004; Dickinson and Snyder 1978). The Great Plains, on the contrary, have remained largely stable since the Precambrian, and so the low Δt^* values here again conform to expectation. Superimposed on this general west-to-east pattern are considerable fluctuations in Δt^* of 0.1 to 0.25 s, mostly within the Wyoming Craton, which agrees with the fact that the Wyoming Craton is not underlain by universally high seismic velocities. The Laramide style deformation that the Wyoming Craton experienced is characterized by discrete, narrow ranges separated by basins (Mueller & Frost, 2006) and, interestingly, the Δt^* flucutations within the Wyoming Craton correlate well with these features. Below, we explore these correlations, focusing on the regions associated with the Black Hills and the Bighorn Arch.

4.2 The Thunder Basin and the Black Hills

Of all the Laramid ranges, the Black Hills is the most isolated from the main trend of the Rocky Mountains; separated by the undeformed region we are referring to as the Thunder Basin. Although the eastern margin of the Wyoming Craton is under debate (the Black Hills, according to Mueller & Frost (2006); or the Bighorn Mountains, according to Kilian et al. 2016 and Worthington et al. 2016), the general consensus is that the Black Hills are another basement cored

uplift like those prevalent in the Rocky Mountains. The Black Hills were uplifted at about 62 Ma (Lisenbee et al., 1993) with several phases of magmatism following until 39 Ma (Kirchner, 1977). Like other Laramide-associated uplifts, the Black Hills feature a high gravity anomaly (Simpson et al., 1986) which could be related to crustal shortening or older basement structures. In contrast, the Thunder Basin remained undeformed during the Laramide Orogeny. Notably, available seismic velocity models (Schmandt & Lin, 2014; Shen & Ritzwoller, 2016) reveal a contrast between the two blocks (Fig. 7A, 7B, 7D). High velocities beneath the TBB extend to depths greater than 300 km (Humphreys et al., 2015), while the Black Hills sit directly above a low-velocity anomaly. The nature of the TBB is under debate: popular interpretations include the downwelling remnants of the Wyoming Craton (Dave & Li, 2016), a remnant of Farallon lithosphere (Wang et al., 2016), and the depleted lithosphere of the Shatsky conjugate (Humphreys et al., 2015). Regardless, these models would all suggest that the lithosphere associated with the Thunder Basin is thicker than that beneath the Black Hills.

In agreement with the velocity models, Δt* is lower in TBB than in BH and the contrast between the two regions (~0.15s) greatly exceeds model uncertainty. While the scattering index reaches a moderate level (0.06) around the north section of BH, the center of BH shows little scattering relative to the regional average (~0). TBB yields a local minimum (~-0.07) in scatter index at the west end, but overall, the scattering fluctuates strongly among nearby stations (Fig. 5b) and the standard deviation is large (~0.08, Figure S7). Considering the high uncertainty in scattering observations, the lateral variation in Δt* is more likely indicative of intrinsic attenuation than of a local maximum in scattering.

Such Δt* variation cannot result solely from variations in sediments or the crust. The TBB is covered by a sedimentary basin, while crystalline basement outcrops in the BH (Shah & Boyd, 2018), so the attenuating sediments would produce the opposite of our observed trend. Moreover, given that the thickness of the sedimentary layer (~3km to the basement for this region) (Shah & Boyd, 2018) is almost negligible compared to that of the highly attenuating asthenosphere, Δt* variation due to sediments should be negligible. Concerning the bulk crust, available Lg attenuation models for the contiguous US (Gallegos et al., 2014, 2017) display little variation among the two blocks. We estimate the maximum Δt* variation generated by Q in the Lg models with a simple block model in Fig. 8a. The Δt* is computed over a range of $\mathbf{Q}_{\mathrm{low}}$, quality factor in the more attenuating crstal block, and crustal thickness h. For simplicity, we assume that $\mathbf{Q_p = 2.25 Q_s}$ (Karato & Spetzler, 1990). As shown in Fig.8a, even if $\mathbf{Q_p}$ is as low as 100 and the crust thickness is 50km, we can only generate 0.06s of Δt*. Such a low quality factor for the crust is unfeasible (Toksöz et al., 1988), and even such unfeasibly low values can explain little of the signal. We reject the crust as the origin of the difference in attenuation.

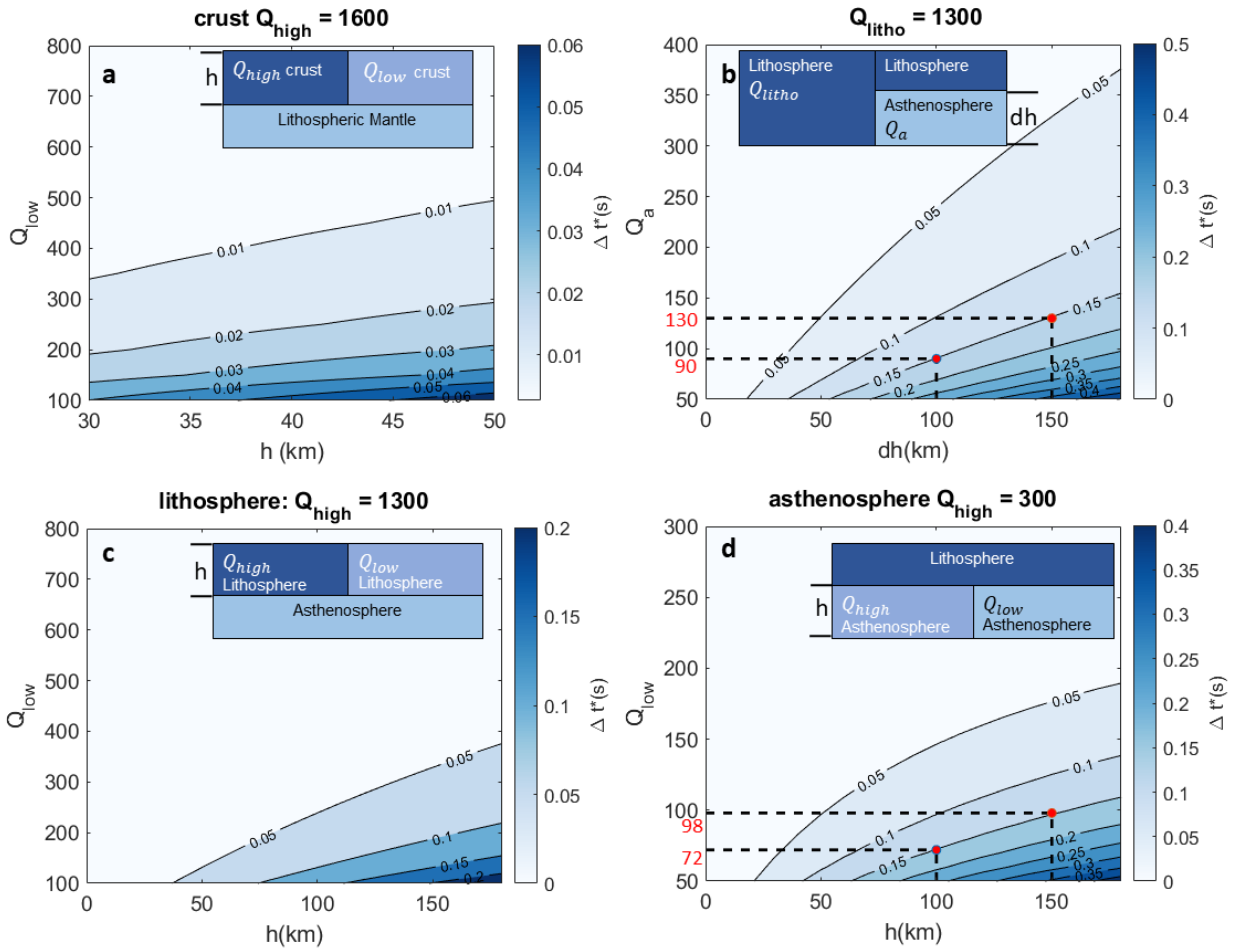

Figure 8. Estimation of Q_p and column thickness under multiple scenarios: (a) h is the thickness of crust, Q_{high} is fixed to be 1600; for each Q_{low} and h pair, we compute how much Δt* can be generated; (b) dh is the variation of lithosphere thickness between two column; Q_a is the Q of underlying asthenosphere; for each dh and Q_a pair, the corresponding Δt* is computed. (c) similar to (a) except that here h is the thickness of the lithosphere, Q_{high} is fixed to be 1300; (d) similar to (a) except that here h represents the thickness of asthenosphere with Q variation. In all cases, Vp of the high Q block is assumed to be 7km/s and the Vp of low Q block is set to be 10% (case (a)), 2% (case (b) and (c)), 0% (case(d)) slower, respectively

Since variations in in lithospheric thickness in the region are well established, we next consider the case of varying lithospheric thickness as a possible explanation for the Δt* contrast. We assume the lithosphere's $\mathbf{Q_p}$ to be 1300 following PREM (Dziewonski & Anderson, 1981), and we compute the corresponding Δt*

for a range of $\mathbf{Q_p}$ in the asthenosphere ($\mathbf{Q_a}$) and the difference in thickness between the two lithospheric columns (dh). The results are presented in Fig.8b and show that 0.15s of Δt* can be reached for a range of dh and $\mathbf{Q_a}$ pairs. For instance, when dh is 150km, we need a $\mathbf{Q_a}$ at ~130, which is a typical value of Q for asthenosphere at 200km depth from the PREM model; if dh is 100km, then $\mathbf{Q_a}$ has to be ~90, which suggests the presence of melt or premelt conditions according to lab experiments, extrapolation calculations and seismic observations (e.g. Abers et al., 2014; Jackson & Faul, 2010; Takei, 2017). Differentiating between these scenarios is beyond the scope of this study, but this calculation shows that the difference in Δt* between the TBB and BH is consistent with a variation in the thickness of the lithosophere of ~100km. Additional observations such as heat flow (Blackwell et al., 2011) and seismic velocity tomography (Schmandt & Lin, 2014; Shen & Ritzwoller, 2016) indicate the Black Hills mark a region of low seismic velocities. The TBB velocity anomaly extends to a depth of ~300km and the slow velocity anomaly (~1% - ~3%) beneath the BH extends from depths of 70 to 300 km. This is consistent with the calculation above that can explain the change in Δt* between the two blocks. A corollary would be that the Black Hills may sit above a weaker and more attenuating zone of the lithosphere, while the surrounding lithosphere is more competent and less attenuating.

4.3 The Bighorn Basin and Bighorn Mountains

The uplifting of the Bighorn Mountains was analgous in many ways to the uplifting of the Black Hills – the Bighorns were raised during the Laramide Orogeny on the western edge of a relatively undeformed basin, the Bighorn Basin (Erslev, 2005). In Fig.7A and Fig.7C, our model shows that the Bighorn Basin features a local minimum in Δt* (~-0.1s) while the Bighorn Mountains display a local maximum in Δt* (~0.1s), marking one of the largest contrasts between neighboring geological units in the map and in clear concordance with the pattern observed at the Black Hills. Contrary to the Black Hills, however, neither currently available tomographic models nor heat flow studies imply elevated temperatures or thinned lithosphere beneath the Bighorn Mountains. Although the northern section of the Bighorn Mountains sits above a 0.5% slow $\mathbf{v_p}$ anomaly at ~200km (Fig. 7C), this anomaly does not extend under the entire mountain range and is missing from the west-east cross-section of Fig. 7B (Shen & Ritzwoller, 2016). We note that currently available regional velocity models are all based on data with a station spacing of ~75km, which makes it hard to image structures with the scale of the Bighorn Mountains (~50km from west to east), and also note that both the Tranportable Array and Global Seismic Networks deployed stations directly within the Black Hills and not directly within the Bighorn Mountains.

In addition to seismic velocity models, we also consider other observations that may suggest the source of Δt* differences. As discussed in the previous subsection, the Δt* contrast in the Bighorn Mountains cannot be explained by fluctutations in sediment thickness (Shah & Boyd, 2018), nor are variations in

crustal Q sufficient to generate such large Δt^*. A possible model of Lg attenuation (Gallegos et al., 2017) does imply sufficient variation in Q between the basin and mountains (400 to 100, respectively), but large disagreements between models constructed with different frequencies implies that scattering produces this contrast (Gallegos et al., 2017). Therefore, we consider several possible scenarios: Δt^* contrast caused by 1) $\mathbf{Q_p}$ variation within the lithosphere (Fig. 8c); 2) $\mathbf{Q_p}$ variation within the asthenosphere (Fig. 8d) 3) variations in lithosphere thickness (Fig. 8b). The method is similar to that presented in Section 4.2, where we perturb the range of Q variations and layer thickness. For case 1), it is not likely that the variations in $\mathbf{Q}_{\text{low}}$ and lithospheric thickness can lead to ~0.15 s difference in Δt^*. For case 2), under certain scenarios (e.g, $\mathbf{Q}_{\text{low}}$ of 72 and layer thickness of 100 km), 0.15s of Δt^* can be explained. Although these values are compatible with geophysical observations (Pozgay et al., 2009; Rychert et al., 2008), the presence of melt is expected for these quality factors (Abers et al., 2014) and so a process for the local production of melt within the Wyoming Craton would be needed. However, no other evidence suggests the presence of melt in this region, because 1) the Bighorn domain experienced limited magmatism prior and post Laramide (Reiners & Farley, 2001); 2) in regions of a similar setting associated with the presence of melt, such as the central Appalachian Mountains, volcanic outcrops (Mazza et al., 2014), extremely high conductivity (Evans et al., 2019) and larger Δt^* contrast (~0.26 s, Byrnes et al., 2019) have been observed. Case 3) appears simpler and is consistent with the discussion in section 4.1, suggesting only a thicker lithosphere underneath the Bighorn Basin. While the lithosphere can in principle vary in both thickness and $\mathbf{Q_p}$, Fig.8 shows that the thickness of lithosphere has a larger impact.

4.4 Implications for Laramide-Style deformation

Motivatived by the above observations and analyses, we speculate that the the interspersed mountains and basins characteristic of Laramide-Style deformation reflect variations in the strength of the lithosphere, which are in turn reflected in Δt^*. Rheological heterogeneities in the lithosphere would, in this view, play a major role in the localization of deformation: the contracting stress produced by the subducting slab would be localized in the regions where the lithosphere is weak and thin, while thicker blocks would have resisted deformation and transferred the stress laterally. The hypothesis is supported by the evident correlation between topography, Δt^*, and seismic velocity structure in the region of the Black Hills and the Thunder Basin. Due to the sensitivity of Δt^* measurements to the structures above a depth of 220 km (Castaneda et al., 2021; Liu et al., 2021), varations in Δt^* are likely due to variations in lithospheric thickness between the different blocks (i.e., Fig. 8).

Variations in the thickness of mantle lithosphere is a distinct mechanism from the typically discussed mechanisms for the localiazation of deformation in this region. Previous studies have typically associated Laramide uplifts with preexisting crustal weaknesses (Erslev & Koenig, 2009), which primarily manifest as faults and undulations in the depth of the Moho as revealed by receiver

functions (Worthington et al., 2016; Yeck et al., 2014). Yeck et al., (2014) in particular gives several hypothetical scenarios, including : 1) the detachment of the crust to the lithospheric mantle under shortening stress, 2) the nucleation of deformation over the preexisting Moho geometry prior to the Laramide Orogeny, 3) the buckling of the entire lithospheric system during compression. These scenarios are not incompatiable with our observations, though our Δt^* results cannot be explained by crustal structure alone. Possibily, prior variations in lithospheric strength contributed to the different response to shortening stress in all these paradigms, such as in a scenario where the crustal-scale weaknesses develop in response to variations in the strength of the mantle lithosphere. The causation is unlikely to run in the opposite direction, where the lithosphere was thinned near zones of crustal weakness. More confidently, models that imply the lithosphere thickens during shortening, such as the "pure-shear thickening" hypothesis where the lower crust thickens beneath mountains (Egan & Urquhart, 1993), predict the opposite correlation between Δt^* and topography that we observed, and therefore can be rejected. On the other hand, we may expect similar Δt^* pattern if the lithosphere thickness variation is a result of Laramide shortening and subsequent delamination events beneath the mountains, but the scenario is less likely considering the small amount of shortening (~20km) at the Black Hills during the Laramide Orogeny (Singleton et al., 2019) and the large contrast in lithosphere thickness compared to TBB.

Our results also speak to the debate on the nature of TBB. The overlap between high velocity anomalies and low Δt^* suggest the TBB is strong and thick, and so more likely to reflect intact lithosphere than an actively delaminating root. In order to explain our results, the delaminating root would need to fill the area of the TBB where we observe low attenuation, instead of collapsing into a narrower column as in geodynamic simulations (e.g. Johnson et al., 2014; West et al., 2009). On the other hand, the recratonization model by Humphreys et al. (2015) cannot be ruled out with our observations, since both cratonic lithosphere and oceanic lithosphere would appear as high-velocity, high-Q bodies, although recratonization would have had to protect the overriding lithosphere from deformation immediately after, or even during emplacement of the allocthonous keel. This recratonization process, though, may not be necessary to account for the thick lithosphere present at TBB, considering the study area's proximity to the ancient Wyoming Craton. The hypothesis that deformation is localized in part by variations in the strength of the upper mantle predicts that this pattern of apparent attenuation could be extrapolated to much of the Rocky Mountains, where the Laramide style deformation is ubiquitous, and other areas showing Laramide-style deformation such as the Sierras Pampeanas (e.g., Ramos et al. 1986). Patterns of this sort have been observed with seismic attenuation in the Iberian Pennsiula (Bezada, 2017) and in Southern China (Deng et al., 2021) where basins have retained their shape during diffuse deformation, but such a pattern has not to our knowledge been previously observed within a recent orogony. We speculate that the lithosphere beneath the basins should be generally thicker than beneath the surrounding mountains in such regions. In contrast, if

pre-existing crustal structure alone can localize deformation, then there need not to be any correlation between uplift and lithospheric thickness in these regions.

5 Conclusions

With time-domain analysis of teleseismic attenuation of first-arriving *P*-phases, we produce a model of Δt* in northern Wyoming and surrounding regions. The Δt* values generally decrease from west to east, which agrees well with previous Δt* studies for the region. Within the Wyoming Craton, we observe higher Δt* in the prominent mountain ranges (the Bighorn Mountains and the Black Hills) and lower Δt* in adjacent basins (the Bighorn and Thunder Basins, respectively). We conclude that the Δt* model primarily reflects variations of intrinsic attenuation in the lithosphere-asthenosphere system, since the results anti-correlate with a proxy for the scattering of the wavefield. We also observe a positive correlation between topography and Δt* with high confidence. In available seismic velocity models, the Black Hills and Thunder Basin are above slow and fast velocity anomalies, respectively, which agrees well with our results. We conclude that the lithosphere beneath the mountains is thinner than that beneath the basins. Considering the tectonic environment and broader scale of deformation during the Laramide Orogeny, the result suggests the stress transferred by pre-existing stronger and thicker lithosphere blocks to weaker zones could have led to the formation of the Black Hills and the Bighorn Mountains. We speculate similar observations could be made in other Laramide ranges if there was sufficiently dense station coverage. We conclude that lateral variations in lithospheric strength and thickness, as evinced by our seismic attenuation measurements, played an important role in the localization of deformation and orogenesis during the Laramide Orogeny.

Acknowledgments, Samples, and Data

This work was funded by the National Science Foundation (EAR-1944998, EAR-1827277), University of Minnesota (Proposal 325013), and University of California, Riverside (Regents Faculty Fellowship). The method and code used in this study has been open-sourced at https://github.com/jsbyrnes/tSToolbox (https://doi.org/10.5281/zenodo.4277716). The dataset containing the seismic data and the corresponding $\mathbf{\Delta}$t* measurements is available at figshare data repository (https://doi.org/10.6084/m9.figshare.14794398). The data from BASE array can be accessed at the IRIS DMC (http://ds.iris.edu/mda/XV/?timewindow=2009-2010), and the data from CIELO array will be released at 2021-12-31.

References

Abers, G. A., Fischer, K. M., Hirth, G., Wiens, D. A., Plank, T., Holtzman, B. K., et al. (2014). Reconciling mantle attenuation-temperature relationships from seismology, petrology, and laboratory measurements. *Geochemistry, Geophysics, Geosystems*, *15*(9), 3521–3542. https://doi.org/10.1002/2014GC005444Azimi, S. A. (1968). Impulse and transient characteristics of media with linear and quadratic absorption laws, Izvestiya. *Phys. of the Solid Earth*, *Feb*, 88–93.Beck, S. L., & Zandt, G. (2002). The nature of orogenic crust in the

central Andes. *Journal of Geophysical Research: Solid Earth*, *107*(B10), ESE 7-1-ESE 7-16. https://doi.org/10.1029/2000JB000124Bezada, M J, Byrnes, J., & Eilon, Z. (2019). On the robustness of attenuation measurements on teleseismic P waves: insights from micro-array analysis of the 2017 North Korean nuclear test. *Geophysical Journal International*, *218*(1), 573–585. https://doi.org/10.1093/gji/ggz169Bezada, Maximiliano J. (2017). Insights into the lithospheric architecture of Iberia and Morocco from teleseismic body-wave attenuation. *Earth and Planetary Science Letters*, *478*, 14–26. https://doi.org/10.1016/j.epsl.2017.08.029Bird, P. (1998). Kinematic history of the Laramide orogeny in latitudes 35°–49°N, western United States. *Tectonics*, *17*(5), 780–801. https://doi.org/10.1029/98TC02698Blackwell, D., Richards, M., Frone, Z., Batir, J., Ruzo, A., Dingwall, R., & Williams, M. (2011). *Temperature-at-depth maps for the conterminous US and geothermal resource estimates*. Southern Methodist University Geothermal Laboratory, Dallas, TX (United States).Bodin, T., Sambridge, M., Rawlinson, N., & Arroucau, P. (2012). Transdimensional tomography with unknown data noise: Transdimensional tomography. *Geophysical Journal International*, *189*(3), 1536–1556. https://doi.org/10.1111/j.1365-246X.2012.05414.xByrnes, J. S., & Bezada, M. (2020). Dynamic Upwelling Beneath the Salton Trough Imaged With Teleseismic Attenuation Tomography. *Journal of Geophysical Research: Solid Earth*, *125*(11), e2020JB020347. https://doi.org/10.1029/2020JB020347Byrnes, J. S., Bezada, M., Long, M. D., & Benoit, M. H. (2019). Thin lithosphere beneath the central Appalachian Mountains: Constraints from seismic attenuation beneath the MAGIC array. *Earth and Planetary Science Letters*, *519*, 297–307. https://doi.org/10.1016/j.epsl.2019.04.045Cafferky, S., & Schmandt, B. (2015). Teleseismic P wave spectra from USArray and implications for upper mantle attenuation and scattering. *Geochemistry, Geophysics, Geosystems*, *16*(10), 3343–3361. https://doi.org/10.1002/2015GC005993Castaneda, R. A. S., Abers, G. A., Eilon, Z. C., & Christensen, D. H. (2021, January 16). Teleseismic attenuation, temperature, and melt of the upper mantle in the Alaska subduction zone [preprint]. https://doi.org/10.1002/essoar.10505839.1Coney, P. J., & Reynolds, S. J. (1977). Cordilleran benioff zones. *Nature*, *270*(5636), 403–406.Conrad, C. P., & Molnar, P. (1997). The growth of Rayleigh-Taylor-type instabilities in the lithosphere for various rheological and density structures. *Geophysical Journal International*, *129*(1), 95–112. https://doi.org/10.1111/j.1365-246X.1997.tb00939.xDave, R., & Li, A. (2016). Destruction of the Wyoming craton: Seismic evidence and geodynamic processes. *Geology*, *44*(11), 883–886. https://doi.org/10.1130/G38147.1DeCelles, P. G. (2004). Late Jurassic to Eocene evolution of the Cordilleran thrust belt and foreland basin system, western U.S.A. *American Journal of Science*, *304*(2), 105–168. https://doi.org/10.2475/ajs.304.2.105DECELLES, P. G., GRAY, M. B., RIDGWAY, K. D., COLE, R. B., SRIVASTAVA, P., PEQUERA, N., & PIVNIK, D. A. (1991). Kinematic history of a foreland uplift from Paleocene synorogenic conglomerate, Beartooth Range, Wyoming and Montana. *GSA Bulletin*, *103*(11), 1458–1475. https://doi.org/10.1130/0016-7606(1991)103<1458:KHOAFU>2.3.CO;2Deng,

Y., Byrnes, J. S., & Bezada, M. (2021). New Insights Into the Heterogeneity of the Lithosphere-Asthenosphere System Beneath South China From Teleseismic Body-Wave Attenuation. *Geophysical Research Letters*, *48*(6), e2020GL091654. https://doi.org/10.1029/2020GL091654Dickinson, W. R., & Snyder, W. S. (1978). Plate tectonics of the Laramide orogeny. In *Geological Society of America Memoirs* (Vol. 151, pp. 355–366). Geological Society of America. https://doi.org/10.1130/MEM151-p355Dziewonski, A. M., & Anderson, D. L. (1981). Preliminary reference Earth model. *Physics of the Earth and Planetary Interiors*, *25*(4), 297–356.Egan, S. S., & Urquhart, J. M. (1993). Numerical modelling of lithosphere shortening: Application to the Laramide erogenic province, western USA. *Tectonophysics*, *221*(3), 385–411. https://doi.org/10.1016/0040-1951(93)90170-OErslev, E., & Koenig, N. (2009). Three-dimensional kinematics of Laramide, basement-involved Rocky Mountain deformation, USA: Insights from minor faults and GIS-enhanced structure maps. *Geological Society of America Memoirs*, *204*, 125–150. https://doi.org/10.1130/2009.1204(06)Erslev, E. A. (2005). 2D Laramide geometries and kinematics of the Rocky Mountains, western U.S.A. *Washington DC American Geophysical Union Geophysical Monograph Series*, *154*, 7–20. https://doi.org/10.1029/154GM02Evans, Rob. L., Benoit, M. H., Long, M. D., Elsenbeck, J., Ford, H. A., Zhu, J., & Garcia, X. (2019). Thin lithosphere beneath the central Appalachian Mountains: A combined seismic and magnetotelluric study. *Earth and Planetary Science Letters*, *519*, 308–316. https://doi.org/10.1016/j.epsl.2019.04.046Fan, M., & Carrapa, B. (2014). Late Cretaceous–early Eocene Laramide uplift, exhumation, and basin subsidence in Wyoming: Crustal responses to flat slab subduction. *Tectonics*, *33*(4), 509–529. https://doi.org/10.1002/2012TC003221Gallegos, A., Ranasinghe, N., Ni, J., & Sandvol, E. (2014). Lg attenuation in the central and eastern United States as revealed by the EarthScope Transportable Array. *Earth and Planetary Science Letters*, *402*, 187–196. https://doi.org/10.1016/j.epsl.2014.01.049Gallegos, A., Ranasinghe, N., Ni, J., & Sandvol, E. (2017). Lg attenuation, frequency dependence and relative site response of the western United States as revealed by the EarthScope Transportable Array. *Geophysical Journal International*, *209*(3), 1955–1971. https://doi.org/10.1093/gji/ggx145Gao, S., Rudnick, R. L., Yuan, H.-L., Liu, X.-M., Liu, Y.-S., Xu, W.-L., et al. (2004). Recycling lower continental crust in the North China craton. *Nature*, *432*(7019), 892–897. https://doi.org/10.1038/nature03162Griffin, W. L., Kobussen, A. F., Babu, E. V. S. S. K., O'Reilly, S. Y., Norris, R., & Sengupta, P. (2009). A translithospheric suture in the vanished 1-Ga lithospheric root of South India: Evidence from contrasting lithosphere sections in the Dharwar Craton. *Lithos*, *112*, 1109–1119. https://doi.org/10.1016/j.lithos.2009.05.015Huang, J., Zhong, S., & Hunen, J. van. (2003). Controls on sublithospheric small-scale convection. *Journal of Geophysical Research: Solid Earth*, *108*(B8). https://doi.org/10.1029/2003JB002456Humphreys, E., Hessler, E., Dueker, K., Farmer, G. L., Erslev, E., & Atwater, T. (2003). How Laramide-Age Hydration of North American Lithosphere by the Farallon Slab Controlled Subsequent Activity in the Western United States. *International Geology Re-*

view, *45*(7), 575–595. https://doi.org/10.2747/0020-6814.45.7.575Humphreys, E. D., Schmandt, B., Bezada, M. J., & Perry-Houts, J. (2015). Recent craton growth by slab stacking beneath Wyoming. *Earth and Planetary Science Letters*, *429*, 170–180. https://doi.org/10.1016/j.epsl.2015.07.066Jackson, I., & Faul, U. H. (2010). Grainsize-sensitive viscoelastic relaxation in olivine: Towards a robust laboratory-based model for seismological application. *Physics of the Earth and Planetary Interiors*, *183*(1), 151–163. https://doi.org/10.1016/j.pepi.2010.09.005Johnson, T. E., Brown, M., Kaus, B. J. P., & VanTongeren, J. A. (2014). Delamination and recycling of Archaean crust caused by gravitational instabilities. *Nature Geoscience*, *7*(1), 47–52. https://doi.org/10.1038/ngeo2019Karato, S., & Spetzler, H. A. (1990). Defect microdynamics in minerals and solid-state mechanisms of seismic wave attenuation and velocity dispersion in the mantle. *Reviews of Geophysics*, *28*(4), 399–421. https://doi.org/10.1029/RG028i004p00399Karato, Shun-ichiro. (2008). Deformation of earth materials. *An Introduction to the Rheology of Solid Earth*, *463*.Kirchner, J. G. (1977). Evidence for Late Tertiary Volcanic Activity in the Northern Black Hills, South Dakota. *Science*, *196*(4293), 977–977. https://doi.org/10.1126/science.196.4293.977Kusky, T. M., & Li, J. (2003). Paleoproterozoic tectonic evolution of the North China Craton. *Journal of Asian Earth Sciences*, *22*(4), 383–397. https://doi.org/10.1016/S1367-9120(03)00071-3Kusky, T. M., Windley, B. F., Wang, L., Wang, Z., Li, X., & Zhu, P. (2014). Flat slab subduction, trench suction, and craton destruction: Comparison of the North China, Wyoming, and Brazilian cratons. *Tectonophysics*, *630*, 208–221. https://doi.org/10.1016/j.tecto.2014.05.028Lee, C.-T. A., Luffi, P., & Chin, E. J. (2011). Building and Destroying Continental Mantle. *Annual Review of Earth and Planetary Sciences*, *39*(1), 59–90. https://doi.org/10.1146/annurev-earth-040610-133505Lisenbee, A. L., DeWitt, E., & Snoke, A. W. (1993). Laramide evolution of the Black Hills uplift. *Geology of Wyoming: Geological Survey of Wyoming Memoir*, *5*, 374–412.Liu, H., Byrnes, J. S., Bezada, M., Wu, Q., Pei, S., & He, J. (2021, May 6). Variable depths of magma genesis in Eastern Asia inferred from teleseismic P wave attenuation [preprint]. https://doi.org/10.1002/essoar.10507202.1Malinverno, A., & Briggs, V. A. (2004). Expanded uncertainty quantification in inverse problems: Hierarchical Bayes and empirical Bayes. *GEOPHYSICS*, *69*(4), 1005–1016. https://doi.org/10.1190/1.1778243Mazza, S. E., Gazel, E., Johnson, E. A., Kunk, M. J., McAleer, R., Spotila, J. A., et al. (2014). Volcanoes of the passive margin: The youngest magmatic event in eastern North America. *Geology*, *42*(6), 483–486. https://doi.org/10.1130/G35407.1Montagner, J.-P., & Kennett, B. L. N. (1996). How to reconcile body-wave and normal-mode reference earth models. *Geophysical Journal International*, *125*(1), 229–248. https://doi.org/10.1111/j.1365-246X.1996.tb06548.xMueller, P. A., & Frost, C. D. (2006). The Wyoming Province: a distinctive Archean craton in Laurentian North America. *Canadian Journal of Earth Sciences*, *43*(10), 1391–1397. https://doi.org/10.1139/e06-075Porter, R., Liu, Y., & Holt, W. E. (2016). Lithospheric records of orogeny within the continental U.S. *Geophysical Research Letters*, *43*(1), 144–153.

https://doi.org/10.1002/2015GL066950Pozgay, S. H., Wiens, D. A., Conder, J. A., Shiobara, H., & Sugioka, H. (2009). Seismic attenuation tomography of the Mariana subduction system: Implications for thermal structure, volatile distribution, and slow spreading dynamics. *Geochemistry, Geophysics, Geosystems*, *10*(4). https://doi.org/10.1029/2008GC002313Ramos, V. A., Jordan, T. E., Allmendinger, R. W., Mpodozis, C., Kay, S. M., Cortés, J. M., & Palma, M. (1986). Paleozoic terranes of the central Argentine-Chilean Andes. *Tectonics*, *5*(6), 855–880. https://doi.org/10.1029/TC005i006p00855Ravenzwaaij, D. van, Moore, C. P., Lee, M. D., & Newell, B. R. (2014). A Hierarchical Bayesian Modeling Approach to Searching and Stopping in Multi-Attribute Judgment. *Cognitive Science*, *38*(7), 1384–1405. https://doi.org/10.1111/cogs.12119Reiners, P. W., & Farley, K. A. (2001). Influence of crystal size on apatite (U–Th)/He thermochronology: an example from the Bighorn Mountains, Wyoming. *Earth and Planetary Science Letters*, *188*(3), 413–420. https://doi.org/10.1016/S0012-821X(01)00341-7Romanowicz, B., & Dziewonski, A. (2010). *Seismology and Structure of the Earth: Treatise on Geophysics*. Elsevier.Rychert, C. A., Fischer, K. M., Abers, G. A., Plank, T., Syracuse, E., Protti, J. M., et al. (2008). Strong along-arc variations in attenuation in the mantle wedge beneath Costa Rica and Nicaragua. *Geochemistry, Geophysics, Geosystems*, *9*(10). https://doi.org/10.1029/2008GC002040Saleeby, J. (2003). Segmentation of the Laramide Slab—evidence from the southern Sierra Nevada region. *GSA Bulletin*, *115*(6), 655–668. https://doi.org/10.1130/0016-7606(2003)115<0655:SOTLSF>2.0.CO;2Schmandt, B., & Humphreys, E. (2010). Complex subduction and small-scale convection revealed by body-wave tomography of the western United States upper mantle. *Earth and Planetary Science Letters*, *297*(3), 435–445. https://doi.org/10.1016/j.epsl.2010.06.047Schmandt, B., & Lin, F.-C. (2014). P and S wave tomography of the mantle beneath the United States. *Geophysical Research Letters*, *41*(18), 6342–6349. https://doi.org/10.1002/2014GL061231Shah, A. K., & Boyd, O. S. (2018). *Depth to basement and thickness of unconsolidated sediments for the western United States—Initial estimates for layers of the U.S. Geological Survey National Crustal Model* (USGS Numbered Series No. 2018–1115). *Depth to basement and thickness of unconsolidated sediments for the western United States—Initial estimates for layers of the U.S. Geological Survey National Crustal Model* (Vol. 2018–1115). Reston, VA: U.S. Geological Survey. https://doi.org/10.3133/ofr20181115Sheehan, A. F. (2009). Collaborative Research: Geometry and kinematics of basement-involved foreland arches:Insights into continental processes from Earthscope. https://doi.org/10.7914/SN/XV_2009Shen, W., & Ritzwoller, M. H. (2016). Crustal and uppermost mantle structure beneath the United States. *Journal of Geophysical Research: Solid Earth*, *121*(6), 4306–4342. https://doi.org/10.1002/2016JB012887Simpson, R. W., Jachens, R. C., Blakely, R. J., & Saltus, R. W. (1986). A new isostatic residual gravity map of the conterminous United States with a discussion on the significance of isostatic residual anomalies. *Journal of Geophysical Research: Solid Earth*, *91*(B8), 8348–8372. https://doi.org/10.1029/JB091iB08p08348Singleton, J. S., Mavor,

S. P., Seymour, N. M., Williams, S. A., Patton, A. I., Ruthven, R. C., et al. (2019). Laramide shortening and the influence of Precambrian basement on uplift of the Black Hills, South Dakota and Wyoming, U.S.A. *Rocky Mountain Geology*, *54*(1), 1–17. https://doi.org/10.24872/rmgjournal.54.1.1Takei, Y. (2017). Effects of Partial Melting on Seismic Velocity and Attenuation: A New Insight from Experiments. *Annual Review of Earth and Planetary Sciences*, *45*(1), 447–470. https://doi.org/10.1146/annurev-earth-063016-015820Toksöz, M. N., Dainty, A. M., Reiter, E., & Wu, R.-S. (1988). A model for attenuation and scattering in the Earth's crust. *Pure and Applied Geophysics*, *128*(1), 81–100. https://doi.org/10.1007/BF01772591Wang, X., Zhao, D., & Li, J. (2016). The 2013 Wyoming upper mantle earthquakes: Tomography and tectonic implications. *Journal of Geophysical Research: Solid Earth*, *121*(9), 6797–6808. https://doi.org/10.1002/2016JB013118Wang, Y., Zhou, L., & Zhao, L. (2013). Cratonic reactivation and orogeny: An example from the northern margin of the North China Craton. *Gondwana Research*, *24*(3), 1203–1222. https://doi.org/10.1016/j.gr.2013.02.011West, J. D., Fouch, M. J., Roth, J. B., & Elkins-Tanton, L. T. (2009). Vertical mantle flow associated with a lithospheric drip beneath the Great Basin. *Nature Geoscience*, *2*(6), 439–444. https://doi.org/10.1038/ngeo526Whitmeyer, S. J., & Karlstrom, K. E. (2007). Tectonic model for the Proterozoic growth of North America. *Geosphere*, *3*(4), 220–259. https://doi.org/10.1130/GES00055.1Worthington, L. L., Miller, K. C., Erslev, E. A., Anderson, M. L., Chamberlain, K. R., Sheehan, A. F., et al. (2016). Crustal structure of the Bighorn Mountains region: Precambrian influence on Laramide shortening and uplift in north-central Wyoming. *Tectonics*, *35*(1), 208–236. https://doi.org/10.1002/2015TC003840Xie, J., Chu, R., & Yang, Y. (2018). 3-D Upper-Mantle Shear Velocity Model Beneath the Contiguous United States Based on Broadband Surface Wave from Ambient Seismic Noise. *Pure and Applied Geophysics*, *175*(10), 3403–3418. https://doi.org/10.1007/s00024-018-1881-2Yeck, W. L., Sheehan, A. F., Anderson, M. L., Erslev, E. A., Miller, K. C., & Siddoway, C. S. (2014). Structure of the Bighorn Mountain region, Wyoming, from teleseismic receiver function analysis: Implications for the kinematics of Laramide shortening. *Journal of Geophysical Research: Solid Earth*, *119*(9), 7028–7042. https://doi.org/10.1002/2013JB010769Zhu, R., Xu, Y., Zhu, G., Zhang, H., Xia, Q., & Zheng, T. (2012). Destruction of the North China craton. *Science China Earth Sciences*, *55*(10), 1565–1587.